Integration of a Graph Network for Landslide Detection in Space-borne Earth Observation

M. A. Luck[1*], **I. Hajnsek**[1,2†]

[1]Institute of Environmental Engineering, ETH Zurich, Rämistrasse 101, 8092 Zurich, Switzerland
[2]German Aerospace Center (DLR) e.V. Microwaves and Radar Institute, Münchener Straße 20, 82234 Weßling, Germany

Key Points:

- A machine learning approach is refined to detect landslides in Sentinel 1 and 2 acquisitions
- A graph network is implemented to describe the neighbourhood of each pixel to train a random forest classifier

[*]Leopold-Ruzicka-Weg 4, 8093 Zurich, Switzerland
[†]Leopold-Ruzicka-Weg 4, 8093 Zurich, Switzerland

Corresponding author: Manuel A. Luck, luck@ifu.baug.ethz.ch

Abstract

Landslides pose a significant threat to society and infrastructure and their occurrence is projected to increase in many regions under the effect of climate change. There is an urgent demand for reliable monitoring of this natural hazard. The combination of spaceborne remote sensing data with state-of-the-art machine learning algorithms offers valuable tools for landslide detection in remote areas. However, a key limitation for the detection lies in the scale factor, especially for methods relying on pixel neighbourhoods. This study presents an innovative methodology which combines a spatial graph with SAR and multi-spectral change products. The graph integrates the flow direction based on the topography into the neighbourhood determination. This unique neighbourhood allows for the preservation of the unique shape and signature of an individual landslide. This paper compares the proposed graph neighbourhood to a common square window approach. Therefore, a RFC is trained with neighbourhood statistics from both approaches and applied to landslides of varying extent. A research area in New Zealand's West Coast region is selected due to the continuous evolution of a single landslide over multiple events. The graph approach shows promising results, particularly for small-scale events which are successfully detected while being missed by the common window approach. Using the graph neighbourhood, we can even detect the smallest visible extent of the landslide at 2-3 pixels (30-45m) width. The main limitation of the proposed approach lies in the quality of the input data. Future work will focus on the improvement of the Sentinel-1 and Sentinel-2 pre-processing.

1 Introduction

Landslides occur in mountainous regions all over the globe. This common and widespread natural hazard is driven by tectonic, climatic, or human factors and the combination thereof. Analysis of a global fatal non-seismic landslide dataset has revealed more than 55 000 people being killed by landslides between 2004 and 2016 (Froude & Petley, 2018). Beyond human losses, there are also significant economic losses due to damaged infrastructure and destruction of livelihoods. Several studies point at increases in frequency and intensity of heavy rainfall events, which are a key trigger for specific types of landslides, as a consequence of climate change (Guha-Sapir et al., 2012; Seneviratne et al., 2012). The number of people exposed to landslide risks is expected to further increase under these conditions in the future (Gariano et al., 2017). When the physical and meteorological triggers of landslides are coupled with anthropogenic factors (e.g., population increases, urbanization of hazardous areas, land use change), negative consequences are even amplified (Araújo et al., 2022; Promper et al., 2015). Thus, there is an urgent need for detection and observation of landslides in order to prevent human losses and minimize damages to infrastructure.

Considering the widespread occurrence of landslides, spaceborne earth observation missions offer the possibility to survey large areas remotely (Zhong et al., 2020; Zhao & Lu, 2018). There are both active and passive remote sensing data available through ESA's Copernicus Programme providing global coverage with high temporal resolution due to very short revisit times (Torres et al., 2012; Drusch et al., 2012). These data have been used in various studies for mapping (Fayne et al., 2019) and observing (Barra et al., 2016; Manconi et al., 2018) active landslides. Zhong et al. (2020) provide a comprehensive review of state-of-the-art landslide mapping using remote sensing highlighting the increasing interest in object-based approaches and automatizing landslide recognition over the past decades. For future improvements in accuracy and reliability, "exploiting the surface spatial structure of landslides with weighted graph algorithms" (Zhong et al., 2020) is considered very promising.

For the automated detection of smaller events, a key obstacle lies in spatial resolution. Common classification approaches integrate the neighbourhood of each pixel. Well-established neighbourhood operations work with adaptive square windows to assess a pixel's surroundings (Aber et al., 2019; Paranjape et al., 1994; Liu & Mason, 2013). Con-

sequently, smaller events are at risk of being overlooked at lower resolution as the neighbourhood statistics may include a relatively larger non-affected area. As higher resolution generally comes at larger costs, it is essential to exploit as much information as possible from available data in order to ensure broad access to high-quality hazard mapping.

Therefore, the aim is to determine the relevant neighbours of each pixel. This paper proposes a method to integrate physical properties of the moving mass into neighbourhood operations. A graph network based on the topography of the observed area is implemented to determine the neighbourhood of each pixel of an acquisition.

Originally, graph theory was used in fields of studies such as biology, linguistics, and logistics optimization. Promoted by advances in computational power, the application of graphs has since been extended to the analysis of spatial issues (Dale & Fortin, 2010; Cheung et al., 2015). Spatial graphs have become an important pillar of geographic information science to examine topological relations between spatial objects (de Almeida et al., 2013). Today, spatial graphs are used in numerous fields of application ranging from ecology and landscape monitoring to urban studies (de Almeida et al., 2013; Cheung et al., 2015; Fortin et al., 2012). "Although geomorphic systems have been depicted as networks, graph theory has seldom been applied" (Heckmann et al., 2015). The application of graphs to natural hazards such as landslides is considered promising.

Generally, a graph can be defined as a mathematical object consisting of two main components, nodes and edges. Nodes are individual points, which are connected by edges. In a spatial context, nodes are used to represent individual objects with specific properties (e.g., landcover patches). Edges are used to describe the topology between the nodes (Dale & Fortin, 2010; Cheung et al., 2015).

In this paper, the proposed graph consists of nodes for each pixel and edges based on the flow direction. Instead of a common n x n window with n2-1 neighbours, a graph-derived neighbourhood consists of neighbourhood pixels which are connected to the seed node in the graph. Thus, only pixels up- and/or downslope (following the flow direction) are included in the calculation of neighbourhood statistics. This reduces the overall area to the topographically relevant pixels. The focus of this approach lies on detecting landslides characterized by flowing movements as described in the updated Varnes classification (Hungr et al., 2014). Finally, a Random Forest Classifier (RFC) is applied to determine affected and unaffected areas (Belgiu & Drăguţ, 2016; Pal, 2005). This classification method consists of multiple decision trees, which can be compared to common thresholding methods. However, the RFC will construct these decision trees based on the training data provided as input. It is a simple, yet transparent method compared to other machine learning approaches (e.g., neural networks) (Maxwell et al., 2018; Lary et al., 2016) and thus suitable for our study, which focuses on the proposed graph neighbourhood.

2 Study Area and Data

2.1 Cook River/Weheka Valley

In this paper, the introduced method is applied to two landslides which occurred between 2016 and 2018 in the Weheka/Cook River Valley, in the West Coast region of New Zealand's South Island. The West Coast region covers a large elevation range from the coast on the west to the main divide of the Southern Alps with its highest point at 3724 m.a.s.l., Aoraki/Mount Cook. The climate of the West Coast region is characterized by large amounts of rainfall (up to 6000 mm median annual rainfall) with the highest rainfalls typically reported in December and a minimum in February. At high elevations even 10 000 mm of annual rainfall are regularly exceeded (Macara, 2016).

Under the impact of climate change, the West Coast region is expected to become even wetter, mainly due to seasonal increases in winter and spring rainfall as well as overall increases of extreme events. Area-average changes of up to 40% increase in precipitation by 2090 are projected under a high-emission scenario (RCP 8.5) (, 2018). The

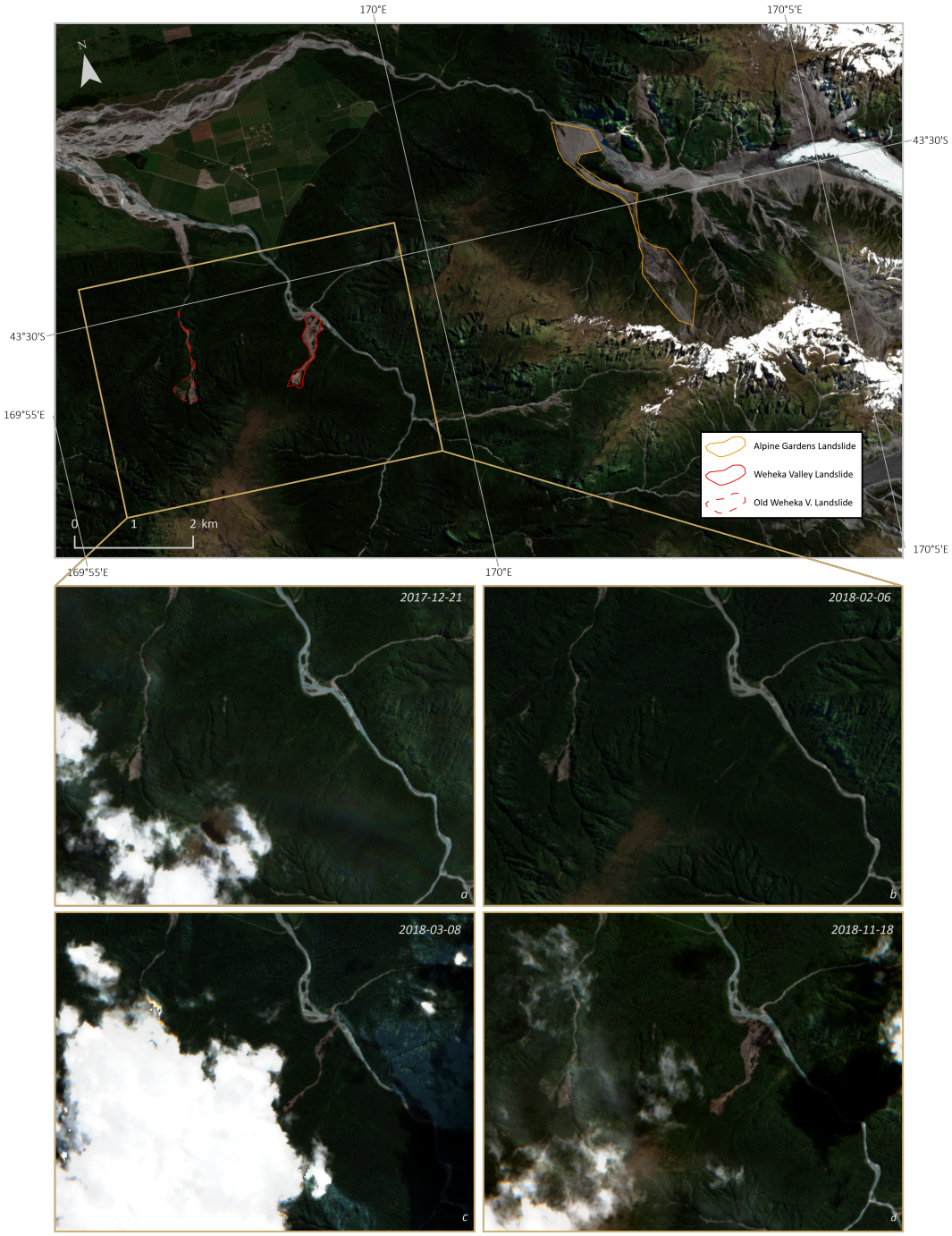

Figure 1. Overview of the research site with a focus on the evolution of the Cook River/Weheka Valley landslide. The four lower images show the Sentinel-2 acquisitions before (a) and after (b) the first and after each subsequent (c-d) event. Furthermore, an older landslide in the Cook River/Weheka Valley as well as the Alpin Garden Landslide are marked as reference points. There are still clouds remaining in the images, due to the lack of cloud-free data. These are partially masked during the pre-processing but still pose one of the largest error sources.

link between heavy rainfall events and the occurrence of landslides is well established. Large parts of the Weheka/Cook River Valley lie within the Westland Tai Poutini National Park, where our research site is located, too. Vegetation is dominated by podocarp-broadleaf temperate rainforest covering the lower parts (Carrivick & Rushmer, 2009) while some sparsely vegetated areas can be found on mountain flanks.

In the northern adjacent Fox Glacier Valley, the Alpine Gardens Landslide, a well-observed and studied area, is located (de Vilder et al., 2020). The entire region is notable for strong erosion, deep-seated gravitational slope deformations as well as numerous landslides which have caused two fatalities and a number of near-misses in the renowned tourist destination. In many cases, the high amounts of rainfall acted as important triggers for these events while some are also linked to their proximity to seismic activity in the Alpine Fault (de Vilder et al., 2022).

In this study, the main event of interest is located at [lat: -43.517, lon: 169.966]. This particular landslide allows for the observation of its evolution from an unaffected forest area to a medium-sized landslide between 28 December 2017 (Figure 1 a) and 18 November 2018 (Figure 1 d). The first visible alterations can be recognized in the Sentinel 2 acquisition on 6 February 2018, where a slim landslide is visible in the valley (approx. 0.02 km^2). During March, the affected area grows in size (approx. 0.12 km^2), and on 18 November 2018 the largest extent (approx. 0.28 km^2) is reached. With continuous data on this development available, we are able to test the proposed graph approach for each stage and extent.

To test the method on a second research site, we apply the approach to another landslide in the same region which occurred one year earlier between 2016 and 2017 [lat: -43.55, lon: 170.0 / approx. 0.02 km^2]. This landslide can be seen on the lower border of the large overview figure, to the right of the 170°E marker. The older Weheka Valley landslide is marked for reference. However, it occurred prior to available Sentinel-1 and Sentinel-2 coverage.

2.2 Data and Software

A strong focus of our work is the easy and flexible applicability for different regions. All data and software used are openly available to make our product available to a broad range of users regardless of financial resources. Regarding the data, we integrate Sentinel-1, Sentinel-2, the Shuttle Radar Topography Mission's (SRTM) digital elevation model (DEM), and landcover products from the Copernicus Land Monitoring Service.

In terms of software, the approach is implemented using Python. For the SAR image processing, the Graph Processing Framework (GPF) included in ESA's SNAP Python API snappy is used. The remaining components of the data are processed with Google Earth Engine's Python API. Furthermore, important libraries comprise GDAL (GDAL/OGR contributors, 2021), NumPy (Harris et al., 2020), and Scikit-learn (Pedregosa et al., 2011) for image co-registration, graph creation, and random forest classification, respectively. All figures are generated using the Matplotlib library. ESA's Sentinel-1 mission provides 1 Interferometric Wide swath (IW) Single Look Complex (SLC) products (i.e., Synthetic Aperture Radar (SAR) Data) with a pixel spacing of 2.3x14.1 m [Range x Azimuth], prior to any multi-looking being performed. The data can be accessed, inter alia, through the Alaska Satellite Facility Vertex. The Sentinel-2 mission acquires high-resolution multispectral data with spatial resolutions of 10m, 20m, or 60m, depending on the bands. In this study, we only integrate the highest resolution bands: B2 (490nm), B3 (560nm), B4 (665 nm), and B8 (842 nm). These are directly accessible through Google Earth Engine's Data Catalog. Both Sentinel missions operate with twin satellites leading to a high temporal resolution (5 days revisit time at the Equator) (Geudtner et al., 2014; Spoto et al., 2012).

Based on the SRTM data, a high-resolution DEM is publicly available at 1 arc-second spatial resolution for regions between 60 degrees north and 54 degrees south latitude.

The data is accessed using the Google Earth Engine (Farr et al., 2007; Gorelick et al., 2017).

Regarding the landcover products, the Copernicus Land Cover Collection (LCC) provides a global surface cover map at 100m resolution, which is annually updated and also accessible through Google Earth Engine's Data Catalog (Buchhorn et al., 2020).

3 Method

We start by presenting the general workflow (see Figure 2), followed by a more detailed description of all processing steps. The workflow can be divided into three main components.

First, there is the data collection and pre-processing workflow for the individual data types. For the SAR data, a Beta-Nought differencing is conducted to observe the changes on the surface between two acquisitions. The optical data is used to calculate a change detection between a cloud-free mosaic of pre- and post-event acquisitions. Second, the implementation of a graph, which is used to merge the data and to calculate neighbourhood operations based on the flow direction, is described in more detail. And third, the classification process is presented. The training of a Random Forest Classifier is explained and the issue of heterogenous landcover affecting the resulting classification is addressed.

3.1 Data Acquisition and Processing

3.1.1 SAR Data Processing

Sentinel-1 IW SLC products with VH polarisation are used for this study. The processing of the SAR data follows the approach used by Mondini et al. (2019), which provides the basis for their photo-interpretation study of numerous landslides worldwide. The approach comprises the calculation of pre- and post-event Beta-Nought images followed by determining the ratio between the images.

The according processing pipeline (Figure 2) consists of the following steps, which are applied to each acquisition using ESA's SNAP Python API snappy: apply orbit file, TOPSAR-split, TOPSAR-deburst, multi-looking (range looks: 4, azimuth looks: 1), speckle-filter (Frost, XY window size: 5, dampening factor: 2), terrain correction (DEM: SRTM 1Sec HGT, image resampling: nearest neighbour, radiometric normalization: save Beta-Nought), and creation of a geographic subset. The two acquisitions are then stacked, and the natural logarithm of their ratio is calculated (Mondini et al., 2019). Furthermore, layover and shadow maps are created during the terrain correction operation. These can be used to mask misleading pixel values.

All SAR data processing steps are implemented using the Graph Processing Framework (GPF) included in ESA's SNAP Python API snappy.

3.1.2 Multi-Spectral Data Processing

In terms of optical data, the study uses the highest-resolution Sentinel-2 bands (i.e., bands: [2,3,4,8]) of the Level-1C product. The data are filtered by orbit and path number in order to minimize geometric distortions between acquisitions. To mask cloud-covered areas, two composites (one pre- and one post-event) are created. The pre-event composite is based on acquisitions during the year prior to the event. Both composites comprise acquisitions for a maximum timespan of four months. However, due to either the need for timely processing or – in our case – the observation of the evolution of the landslide across several stages, the post-event timespan can be reduced accordingly, up to only one single acquisition. While working with a short timespan is possible, this should be done with caution due to a high risk of cloud artifacts. The composites are created by apply-

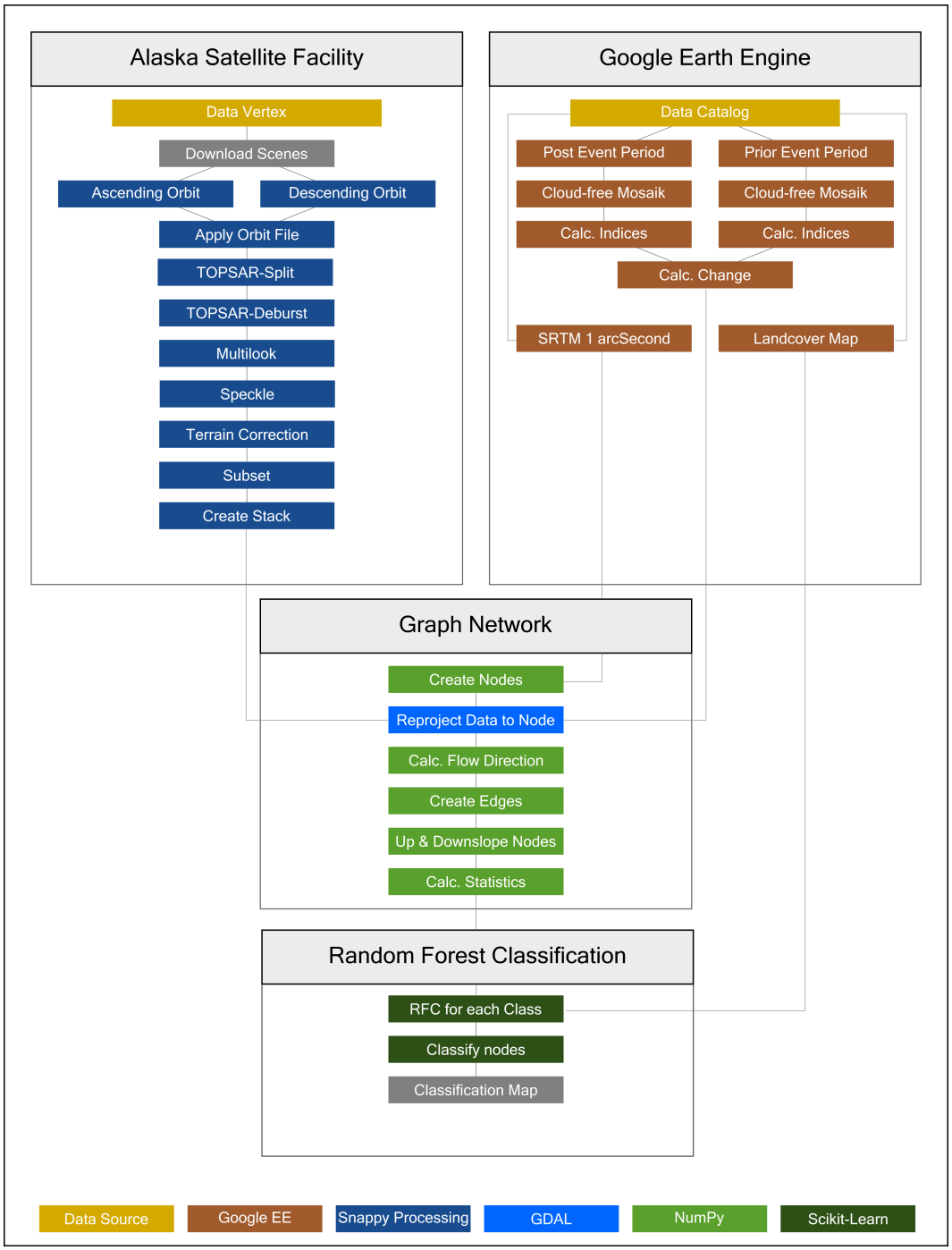

Figure 2. Workflow chart, divided into 4 separate steps and coloured by processing type.

ing a cloud mask to each acquisition and calculating the median of the remaining non-masked values.

Based on these two composites, normalized difference of the chosen bands are calculated to determine the change. As discussed by Fayne et al. (2019), the change in the red band (band 4) indicates the exposure of bare soil, while the change in the SWIR band (band 8) indicates soil moisture change. Furthermore, the NDVI change (Baret et al., 1989) is integrated to allow for a more specific description of vegetation change.

All calculations are performed on the Google Cloud Platform accessed through the Google Earth Engine's Python API (Gorelick et al., 2017). The interim results are then converted to NumPy arrays (Harris et al., 2020), which are integrated into the graph creation.

3.2 Graph Network

The proposed graph aims to enhance the representation of neighbourhood to capture the unique shapes of landslides during the image classification. This improves common moving window approaches, which operate with fixed geometries and weights to determine the neighbours and their relevance.

A graph consists of nodes, which contain specific attributes and edges. Edges describe the connections between the individual nodes. In this application, we assign a node to each pixel of an image. Initial properties of each node comprise the node's ID, the image coordinates, and the node IDs of the neighbouring pixels. Geographic coordinates, height above sea level, slope, aspect, landcover class, and the selected bands of the optical composites and SAR acquisitions are directly added from the input data.

The edges are then created according to the flow direction. Determining the flow direction can be achieved in multiple ways. On the one hand, one could use the aspect derived from the SRTM with Google Earth Engine ee.terrain.aspect() function (Gorelick et al., 2017). On the other hand, the steepest slope within each of the node's neighbours can be calculated and the nodes are then connected accordingly. In this study, we opt for the manual computation due to some artifacts in the aspect calculation on our research site. However, in terms of time efficiency the Google Earth Engine variant would be superior.

The result is a list containing all edges of the graph, further referred to as an "edgelist". The neighbours are defined by searching for the node's ID in the edgelist. Depending on whether the ID is marked as target or origin in the edgelist, one can determine if the neighbour is either up- or downslope of the node. The neighbourhood can be further expanded by recursively running this operation for a chosen number of recursions. This allows for the integration of smaller and larger areas respectively. The resulting neighbourhood accounts for the topography and therefore the movement patterns of most flowing landslides.

When calculating neighbourhood statistics, this method allows for distinct results for up- and downslope as well as their combination. This could be further beneficial for the subdivision of the landslide into multiple areas (e.g., foot, crown, and main body). In this study, only the combined statistics are used due to a lack of detailed training data. In addition, a direct comparison with a common window approach can be made in order to highlight and quantify the benefits of our approach.

The graph is implemented in Python using the open-source libraries NumPy (Harris et al., 2020) and GDAL (GDAL/OGR contributors, 2021).

3.3 Classification

The spectral signature of a landslide is highly variable and depends on the landcover prior to the event. To account for this, we divide the research area into patches of similar landcover types. This subdivision is based on Copernicus' LCC product. To ensure flexible application to any research site, several Random Forest Classifiers (RFCs)

Table 1. Statistics of the change bands for the largest event comparing the overall (tot) and cropped to the reference area (ref) data.

Descending $\beta 0$	min	max	mean	std
tot	-33.51	20.14	-0.10	4.50
ref	-14.68	8.92	-1.10	3.41

Ascending $\beta 0$	min	max	mean	std
tot	-23.38	35.16	-0.79	4.19
ref	-19.69	10.18	-2.77	3.77

are to be trained, one for each patch. As the landslides in our research site only occur in forested areas, the focus of this study lies on one RFC for this landcover type.

The RFC is trained with hand-drawn polygons of the affected area and equally distributed points within the unaffected area. We use the landslide from our second research site for the training as its size is most suitable to represent landslides at which our approach targets. Sentinel-1 and Sentinel-2 derived pixel data and respective neighbourhood statistics are integrated into the training of the RFC. Beyond the combined dataset (SAR and optical data) used for this study, there is also the option to use either of the single datasets (SAR or optical data) depending on the application purpose. The resulting map consists of four classes: affected area, unaffected area, no training for landcover class, and no data.

The classification is implemented in Python using the libraries NumPy (Harris et al., 2020) and Scikit-learn (Pedregosa et al., 2011).

4 Results

4.1 Data Acquisition and Processing

4.1.1 SAR Data Processing

The SAR processing of the main event results in amplitude difference maps for both ascending and descending orbit covering the period of the medium and large stages of the landslide. The smallest stage is only covered by the ascending orbit due to a gap in coverage by the descending orbit between 16 October 2017 and the 7 April 2018. For visualization purposes, Figure 3 g-l show the Beta-Nought of the first acquisition after the respective stages of the landslide. As the landslide occurs on a north-east facing slope, the ascending orbit is more suitable for a visual interpretation due to the stronger foreshortening effect in the descending acquisitions. Visually, only a slight reduction in the amplitude can be observed in the upper part of the landslide at its largest stage. The difference between the acquisitions is used as input data for the RFC.

The same data processing was applied to the research site of the second landslide, which occurred between 2016 and 2017. However, visual detection is unsuccessful. This can be explained by the small extent of the landslide which led to similar issues for smaller stages of the main event.

A comparison of image statistics between the entire acquisition and the affected area is shown in Table 1.

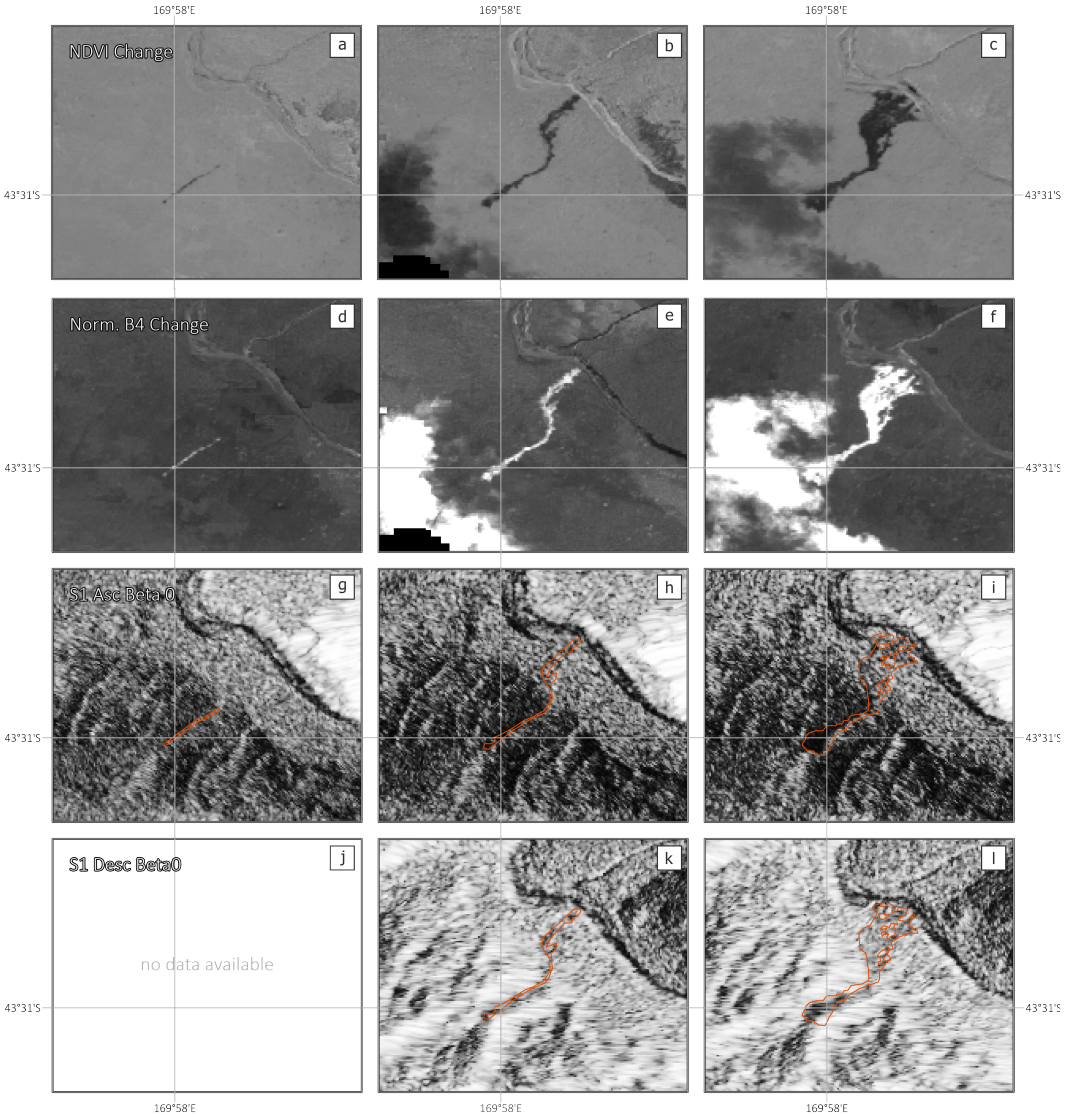

Figure 3. Result subplots showing selected bands of the Multi-Spectral and SAR data processing. Left to right displays the different dates (02.06.2018, 03.08.2018, 11.18.2018) of the main landslide with increasing extent. In the top row, changes in NDVI with a color-range from white (1) to black (-1) are displayed. The second row shows the normalized B4 change with a color-range from white (5) to black (-1). The bottom two are SAR Beta0 layers with the top one being ascending orbit and the lower one descending orbit. The colors of the SAR images range from white (-1dB) to black (-25dB).

4.1.2 Multi-Spectral Data Processing

A clear visual distinction between the landslide and its surrounding vegetated area can be made when looking at the normalized change of the respective bands and the NDVI change. It is even possible to visually recognise the smallest stage of the main event in the product of 6 February 2018 (Figure 3 a, d).

The main visually recognizable changes, which are not caused by the landslide, are due to changes in cloud coverage and sun position. As the time period covered by the acquisitions before the event may be longer than the post-event coverage, cloud/haze relicts are more likely to occur in the post-event cloud-free composite. Therefore, change due to cloud coverage is caused by the appearance, as opposed to the disappearance, of clouds. However, complete coverage without clouds was not possible due to the climate in our study area as well as the fact that one cannot use images acquired after the next largest stage of the landslide. These would not be representative of the studied landslide extent. In addition, there are some misleading changes caused by shadow effects, either due to clouds or differences in the position of the sun (azimuth and zenith) during the composite creation prior to and post-event.

4.2 Graph Network

The visual inspection of the graph (see Figure 4) indicates that the proposed edge creation method results in a robust neighbourhood determination, which takes the flow direction well into account. Thus, the graph can be considered a promising tool to integrate the topography of the research area into the automated detection process. Figure 4 highlights that the edges (depicted as lines) follow the topography and merge in main flow channels. This is also reflected by the line width of the edges which is determined by the number of nodes connected upslope with the seed node within the chosen distance. The thicker the line, the larger area of the contributing flow. The correlation between the edge direction and the flow of the studied landslide is visualized in Figure 4. In particular, the lower parts of the landslide depict this well as the flow is redirected due to elevated areas.

The effect of the graph on the neighbourhood statistics is shown in Figure 5. For reference, the original data is displayed in Figure 5a. Figure 5b displays the mean NDVI calculated using neighbourhood determined by the graph, while 5c displays the mean NDVI calculated using a common square window. All data are normalized to a range from -0.2 to 0.2 with the minimum displayed in red and the maximum in blue. The maximal distance of the graph neighbourhood corresponds to the window size to allow for a direct comparison. Here, a maximum of three iterations up- and downslope of the seed node and a respective 7x7 window size are used. While the common window approach almost entirely blurs shape and signature (value range) of the landslide at its smallest stage, the mean NDVI derived with the graph preserves the shape and intensity (value range) of the original NDVI data (value range).

The boxplots in Figure 6 show the value distribution of the optical change data for the original data, the graph derived mean values and the common window derived mean values within the hand-drawn polygon of the landslide's smallest extent. For reference, the Figure also includes the overall optical image statistics. The comparison between the graph neighbourhood and window neighbourhood derived mean values shows that the results derived from the graph neighbourhood show more similarities in terms of distribution and value range to the original data. Furthermore, the distribution within the window-smoothed data is compressed due to the blurring effect. Thus, the boxplots illustrate the preserving effect of the graph on the original data.

Even though the benefit of the graph neighbourhoods seems more pronounced for small-scale events, Figure 4 shows that the graph leads to a more precise representation of the actual shape of the landslide compared to the common window. Thus, we consider the application of the graph advantageous for neighbourhood representation in this

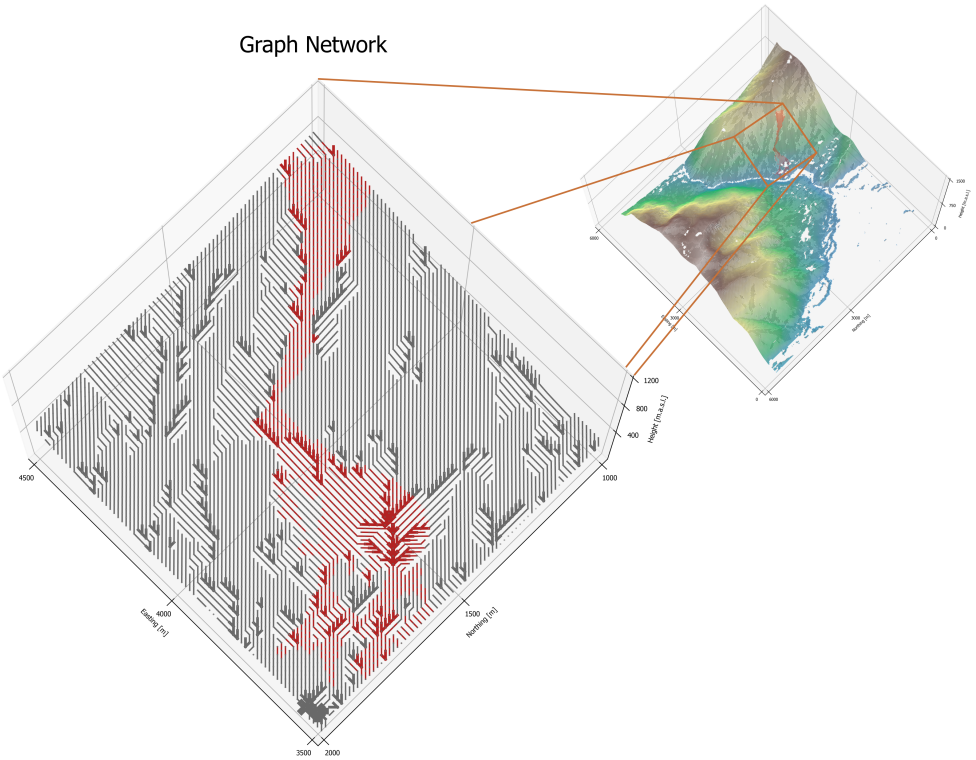

Figure 4. Subset of the graph network, displaying the surroundings of the Weheka Valley landslide with nodes and edges coloured by the reference area. Nodes which are affected by the landslide are coloured in red. A larger linewidth indicates a larger number of upstream nodes connected to the seed node. Top right shows a larger extent with all nodes coloured according to their height for a better understanding of the topography.

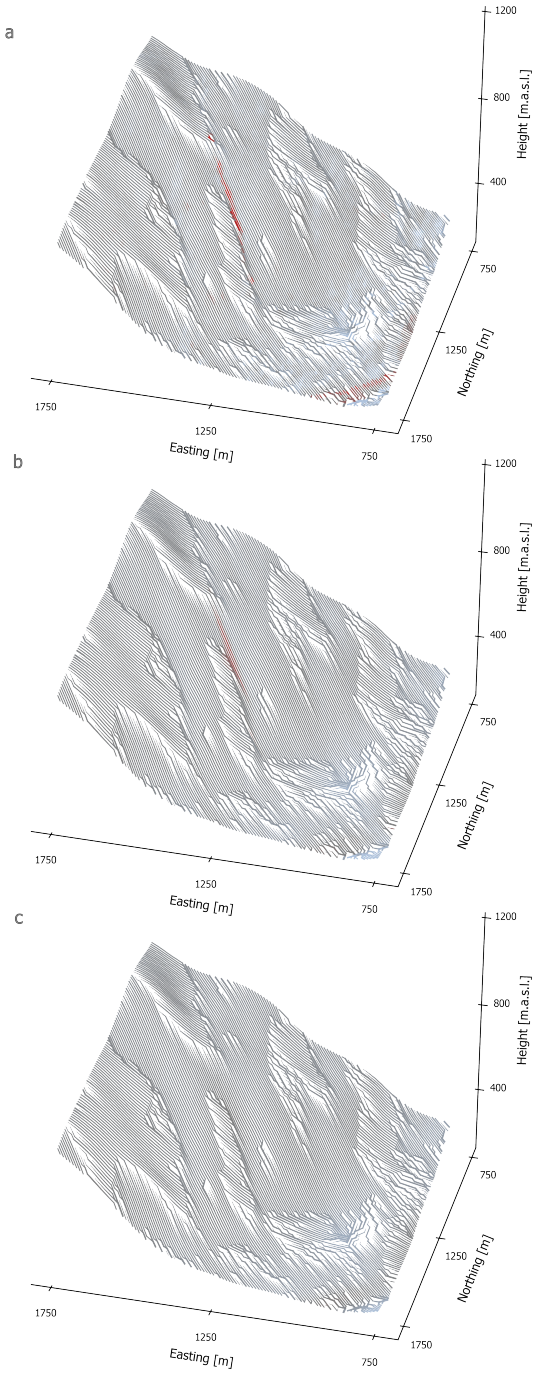

Figure 5. Visualization of the difference between the graph neighbourhood and window neighbourhood mean values. Red indicates negative NDVI change while grey indicates no change. Few blue values at the lower margin indicate positive change. All values are normalized between -0.2 and 0.2 to allow for direct comparisons. The smallest extent of the main landslide is depicted.

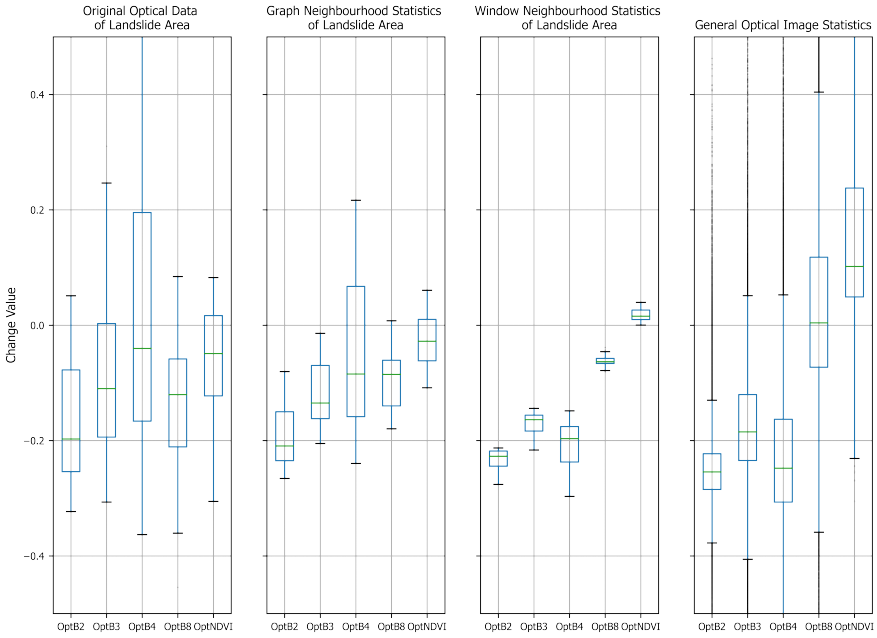

Figure 6. Boxplots illustrating the distribution of the optical data. Left to right: Original data with no filter applied, mean values calculated within the graph neighbourhood, mean values calculated within a square window neighbourhood, and the overall distribution. The first three consider only pixels within the hand-drawn polygons.

Table 2. Accuracy metrics of all classifications. Overall Accuracy (OA), Producer's Accuracy (PA) for affected areas, and User's Accuracy (UA) for affected areas. The overall accuracy is strongly affected by the large proportion of unaffected pixels in the research area. The Producer's Accuracy of the affected area is of particular interest. This metric shows how much of the area marked as landslide in the reference data is actually classified as affected area.

	Graph			Window		
Event	OA	PA	UA	OA	PA	UA
2017-02-08 (second site)	99.92%	80.42%	65.90%	99.89%	80.07%	55.58%
2018-02-06 (smallest main event)	99.98%	25.35%	94.74%	99.97%	0%	NaN
2018-03-08 (medium main event)	91.47%	96.01%	2.49%	93.88%	99.8%	3.56%
2018-11-18 (largest main event)	97.80%	100%	19.16%	99.34%	98.70%	43.97%

research area. No drawbacks could be determined compared to the common window approach besides the higher computational demand.

4.3 Classification

The results of the classification support our findings from the comparison between the graph and window neighbourhood. In particular, smaller events are successfully detected using the graph and likely to be missed by a common window approach. Figure 7 displays the classification results for both the graph and the window approach with the hand-drawn verification polygons and the NDVI change for reference. The comparison between the different observations reveals that the classification using the graph neighbourhood represents the shape of the landslide more accurately than the window approach in all cases. This clearly points out one of the main benefits of the graph in this study. These findings are also supported by the accuracy metrics (see Table 2. The overall accuracy lies above 90% for all events and both approaches. This is due to the large number of unaffected pixels in our research area. Comparing the Producer's Accuracies between the graph and the window approach, it is striking that the graph outperforms the window approach in three out of four cases. Regarding a direct comparison between the accuracy metrics with those from other studies, one must keep in mind that these metrics are calculated on a pixel- rather than object-basis.

Looking at Figure 7, in particular the top and the bottom rows show high accuracies in the classification of the landslides. These classifications also benefit from almost cloud-free input data. It is striking that the small landslide in the bottom row is only detected using the graph approach and missed with the common window. The classifications of the remaining two extents include more false positive values. These can be traced back to cloud (see purple square, Figure 7) and shadow (see yellow square, Figure 7) effects as discussed for the optical data. The window approach outperforms the graph approach regarding overall accuracy of these classifications as it obscures smaller areas which are affected by shadow or clouds. In general, this highlights that the graph approach is most promising when the input-data can be improved (e.g., by more sophisticated shadow / cloud removal) as well as for landslides of small extents. The smallest extent of the landslide (Figure 7, bottom row) has an approximate diameter of 30-45m, which corresponds to a width of 2-3 pixels/nodes as shown in the subplot on the right.

5 Discussion

The proposed approach represents an innovative methodology to improve automated landslide detection by integrating the topography into neighbourhood operations. The implementation of a graph allows for an enhanced description of the pixel neighbourhood

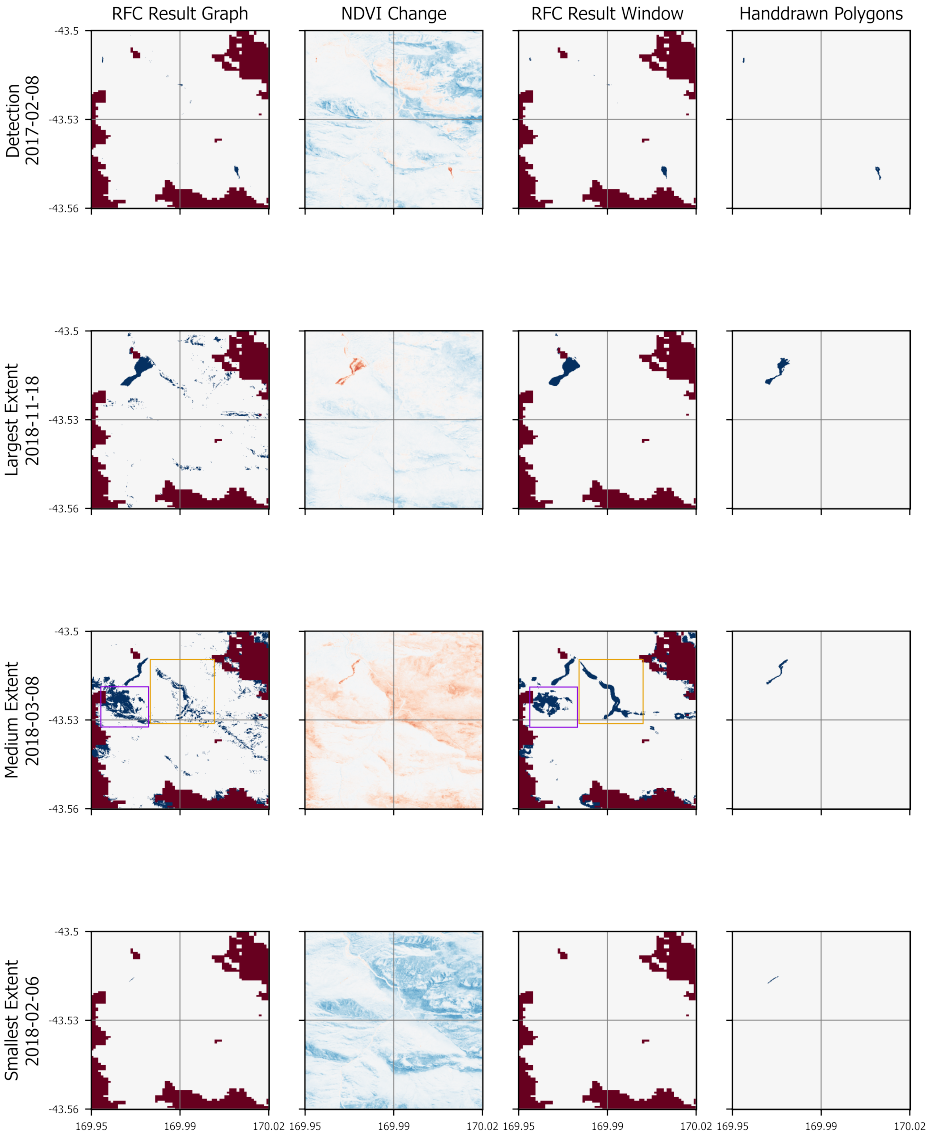

Figure 7. Random Forest Classification results. Top to bottom: Second research area/period (2016/17), largest extent of the main event, medium extent of the main event, and smallest extent of the main event. Left to right: RFC results using the graph neighbourhood, NDVI change for orientation, RFC results using the window neighbourhood, and handdrawn polygons for verification. Areas colored in blue in the RFC results are classified as affected areas, white as unaffected and red as areas with another land cover class. The NDVI change values are colored from red (-1) to blue (1). Areas marked with a yellow square show misclassified values due to hillshadow differences between the composites.Purple squares highlight areas affected by cloud cover.

as compared to a common window approach. As shape and signature of a landslide are better preserved using the graph (see Figure 5), we are able to reduce the size limitation of detectable events. For small scale events, this effect is particularly pronounced (see Figure 6). Effectively, this allows for a broader application of landslide detection with spaceborne remote sensing. Given the widespread occurrence of small-scale landslides (Corominas & Moya, 2008), which is projected to further increase under climate change (Collison et al., 2000), improvements in their detection are highly valuable to prevent human and economic losses.

Both SAR and optical open-source remote sensing products are combined to exploit the benefits of each data type. While higher-resolution products are available in terms of both SAR (e.g., TanDEM-X) and optical data (e.g., Airbus SPOT 6/7), a conscious decision to work with open data was made. We regard it as essential to provide broad access to our findings to ensure its applicability in natural hazard mitigation and response regardless of financial resources. The use of Sentinel-1 and Sentinel-2 products limits the approach to events which occurred after 2016. This leads to some obstacles in terms of availability of training data as most entries of landslide catalogues date to a timespan before Sentinel-1 and Sentinel-2 availability (e.g., U.S. Landslide Inventory (Jones et al., 2019), New Zealand Landslide Database (Rosser et al., 2017)). However, as the application of our approach is aimed to help in hazard mitigation and response, recent and future landslides are the most common application scenarios and thus not affected by this limitation.

In terms of data quality, the main concern with the optical data relates to cloud artifacts in the composites. These could be identified as the main source of error during the classification process. Therefore, future improvements could include more sophisticated cloud masking algorithms. Various promising approaches based on Sentinel-2 data exist (Zekoll et al., 2021; Candra et al., 2020; Tarrio et al., 2020). Or one could specifically train changes due to cloud cover as an additional class in the RFC. Furthermore, shadow effects due to acquisition geometry changes and sun position cause some artifacts as well. Generating hillshades with the Google Earth Engine (Gorelick et al., 2017) for each Sentinel-2 acquisition and the respective sun position is expected to reduce these artifacts.

The comparison between Sentinel-1 and Sentinel-2 data availability reveals the striking effect of cloud coverage reducing the availability of usable optical imagery. Aiming to provide a quick classification map after an event, the length of the post event period utilized for the optical cloud free mosaic is a key limitation of this approach. This is particularly problematic for the study of rainfall-induced landslides, where cloud coverage can delay the availability of cloud-free images significantly. The use of SAR data can avoid this issue. However, in our forested study area even the largest stage of the landslide was barely visible in the SAR data (see Figure 3). Based on Mondini et al. (2019), this could be expected as their manual interpretation of SAR imagery only provided a delineated landslide area for 8 out of 32 events, which were all larger in size compared to all stages of the landslide we study. In order to ensure our approach's applicability to a wide range of research sites with unique properties, the SAR data is still included. This could prove especially beneficial for application in bare soil or rock environments, where optical change is less clear. Furthermore, other SAR products such as coherence change (Tzouvaras et al., 2020), Coefficient of Variation (Colin Koeniguer & Nicolas, 2020), or the use of polarimetric ratios (Plank et al., 2016) could provide valuable additional information. In addition, regarding the fast-paced advances in satellite missions, the integration of multi-frequency SAR acquisitions (Turkar et al., 2012) could be of great interest for the future, in particular for the integration of more landcover types into the study.

A key limitation of the study lies in the training data which stem from a forested area only. This can be regarded problematic as no other landcover types are integrated at the current state of our approach. However, the main goal was to highlight the effect of the graph neighbourhood on the classification process rather than the presentation of a trained random forest classifier for landslide detection. Future work will aim at the

integration of various landcover types in order to provide a more sophisticated tool. This will be accompanied by the previously mentioned changes in the processing of the earth observation data. Besides the training on other landcover types, one could also train the RFC for individual parts of a landslide (e.g., foot, main body, crown)(Griffiths, 2018). The distinction between up- and downslope neighbours in the graph neighbourhood could provide valuable information which bears great potential. The distinction between different landslide parts has been rarely integrated into landslide detection (Zhong et al., 2020). The few existing studies on this topic rely on high-resolution LiDAR data (Glenn et al., 2006; Deng & Shi, 2014; Van Den Eeckhaut et al., 2012).

In terms of LiDAR data, the integration of higher resolution DEMs would be beneficial for increasing the accuracy of the derived flow direction and therefore the neighbourhood statistics. The main advantage of the SRTM used in this study lies in near-global coverage and easy open access. For more targeted applications of the approach, locally available products should be considered. Various countries provide highly detailed and time-sensitive products, provided by e.g., LINZ, USGS, or Swisstopo. Furthermore, a similar product to the SRTMs DEM is the produced by the TanDEM-X mission at higher resolution with DEMs available for multiple years (Zink et al., 2014). Besides the flow direction's dependency on the data resolution, further improvements could also include the implementation of more sophisticated algorithms to derive the flow direction, e.g., the D-Infinity flow direction by Tarboton (1997).

As graph theory has not been commonly applied for landslide detection (Heckmann et al., 2015), the possibility for direct comparison to similar studies is limited. In the future, it would be interesting to investigate possibilities to integrate common graph measures such as connectivity or betweenness. These are frequently used in applications of graph theory but have not been integrated into our approach yet. In particular, such measures could be useful for the combination of susceptibility mapping (Hong et al., 2007) and landslide detection.

Furthermore, most studies using remote sensing for landslide detection either work with single events of larger extents or apply their methodology to large areas with numerous smaller events (Stumpf & Kerle, 2011; Fayne et al., 2019). To demonstrate the benefits of our work, we train the RFC with data derived from both the graph and a common window neighbourhood. This resulted in the accuracy metrics displayed in Table 2. Particular note should be given to smaller events, which were successfully detected using the graph approach while being overlooked when using the common window neighbourhood (see Figure 7). It is also important to keep in mind that false-positive detection is preferable to false-negative detection regarding disaster response.

Our results highlight the potential of a graph neighbourhood compared to a common window approach. The graph can be easily integrated into studies using neighbourhood operations and is considered promising to improve the accuracy of landslide detection. Most misclassified pixels can be traced back to well-studied phenomena (e.g., shadow effects). Therefore, the discussed improvements are expected to enhance the classification accuracy in the future.

6 Conclusion

A graph describing the topography of the observed area is successfully implemented to determine the neighbourhood of each pixel of an acquisition and compared to a common square window neighbourhood. This allows for the integration of the physical properties of the moving mass into the landslide detection process with remote sensing data. The key benefit of the proposed graph lies in the preservation of the shape and signature of the landslide's change in earth observation data, even at very small scales (2-3 pixels width). This can be highly valuable for applications of automated classification in machine learning, which integrate the neighbourhood. Regarding the urgent global demand for improved hazard mitigation, particularly in remote areas, the proposed ap-

proach could provide a valuable tool to exploit as much information as possible from available and affordable data.

Applying a RFC, we demonstrate that the graph neighbourhood allows for the detection of smaller events compared to a common square window. The RFC achieves high accuracy values if given high-quality input data. At the current stage of the approach, the key limitation lies in the pre-processing and/ or availability of data. Future work will be aimed at the integration of more sophisticated cloud removal techniques as well as masking changes in hillshadows due to differences in the sun position between acquisitions. Further improvements are expected from the inclusion of additional landcover types in the training of the RFC. This could come hand in hand with the integration of data products such as coherence change between two Sentinel-1 acquisitions.

Open Research

The Copernicus Sentinel-2 data used for calculating the spectral changes in the study are available at the earth engine data catalog via `https://developers.google.com/earth-engine/datasets/catalog/COPERNICUS_S2#description` with free, full, and open access. The Copernicus Sentinel 1 data used for calculating the amplitude changes in the study are available at the Alaska Satellite Facility (ASF) Search Vertex via `https://search.asf.alaska.edu/#/` and processed by ESA with free, full, and open access. The SRTM data used for the geocoding of the nodes of the graph network in the study are available as auto-download in the SNAP software via `http://step.esa.int/auxdata/dem/SRTMGL1/`.

Acknowledgments
The authors would like to thank all data providers and their staff for the free provision of data. Furthermore, the authors would like to thank the editors and reviewers of the AGU Journals for their contributions in this publication.

References

M. f. t. E. (2018). Climate change projections for new zealand: Atmosphere projections based on simulations from the ipcc fifth assessment, 2nd edition.

Aber, J. S., Marzolff, I., Ries, J., & Aber, S. E. W. (2019). *Small-format aerial photography and uas imagery: Principles, techniques and geoscience applications.* Academic Press.

Araújo, J. R., Ramos, A. M., Soares, P. M. M., Melo, R., Oliveira, S. C., & Trigo, R. M. (2022, 6). Impact of extreme rainfall events on landslide activity in portugal under climate change scenarios. *Landslides*. doi: 10.1007/S10346-022-01895-7

Baret, F., Guyot, G., & Major, D. (1989). Crop biomass evaluation using radiometric measurements. *Photogrammetria*, *43*(5), 241–256. doi: https://doi.org/10.1016/0031-8663(89)90001-X

Barra, A., Monserrat, O., Mazzanti, P., Esposito, C., Crosetto, M., & Scarascia Mugnozza, G. (2016). First insights on the potential of sentinel-1 for landslides detection. *Geomatics, Natural Hazards and Risk*, *7*(6), 1874–1883. doi: https://doi.org/10.1080/19475705.2016.1171258

Belgiu, M., & Drăguţ, L. (2016). Random forest in remote sensing: A review of applications and future directions. *ISPRS journal of photogrammetry and remote sensing*, *114*, 24–31. doi: https://doi.org/10.1016/j.isprsjprs.2016.01.011

Buchhorn, M., Smets, B., Bertels, L., De Roo, B., Lesiv, M., Tsendbazar, N.-E., ... Fritz, S. (2020, September). Copernicus global land service: Land cover 100m: collection 3: epoch 2017: Globe.
doi: https://doi.org/10.5281/zenodo.3518036

Candra, D. S., Phinn, S., & Scarth, P. (2020). Cloud and cloud shadow masking for sentinel-2 using multitemporal images in global area. *International Journal of Remote Sensing*, *41*(8), 2877–2904. doi: https://doi.org/10.1080/01431161.2019.1697006

Carrivick, J. L., & Rushmer, E. L. (2009). Inter-and intra-catchment variations in proglacial geomorphology: an example from franz josef glacier and fox glacier, new zealand. *Arctic, Antarctic, and Alpine Research*, *41*(1), 18–36. doi: https://doi.org/10.1657/1523-0430-41.1.18

Cheung, A. K. L., O'sullivan, D., & Brierley, G. (2015). Graph-assisted landscape monitoring. *International Journal of Geographical Information Science*, *29*(4), 580–605. doi: https://doi.org/10.1080/13658816.2014.989856

Colin Koeniguer, E., & Nicolas, J.-M. (2020). Change detection based on the coefficient of variation in sar time-series of urban areas. *Remote Sensing*, *12*(13), 2089. doi: https://doi.org/10.3390/rs12132089

Collison, A., Wade, S., Griffiths, J., & Dehn, M. (2000). Modelling the impact of predicted climate change on landslide frequency and magnitude in se england. *Engineering Geology*, *55*(3), 205–218. doi: https://doi.org/10.1016/S0013-7952(99)00121-0

Corominas, J., & Moya, J. (2008). A review of assessing landslide frequency for hazard zoning purposes. *Engineering geology*, *102*(3-4), 193–213. doi: https://doi.org/10.1016/j.enggeo.2008.03.018

Dale, M., & Fortin, M.-J. (2010). From graphs to spatial graphs. *Annual Review of Ecology, Evolution, and Systematics*, *41*, 21–38. doi: https://doi.org/10.1146/annurev-ecolsys-102209-144718

de Almeida, J.-P., Morley, J., & Dowman, I. (2013). A graph-based algorithm to define urban topology from unstructured geospatial data. *International Journal of Geographical Information Science*, *27*(8), 1514–1529. doi: https://doi.org/10.1080/13658816.2012.756881

Deng, S., & Shi, W. (2014). Semi-automatic approach for identifying locations of shallow debris slides/flows based on lidar-derived morphological features. *International Journal of Remote Sensing*, *35*(10), 3741–3763. doi: https://doi.org/10.1080/01431161.2014.915438

de Vilder, S., Massey, C., Archibald, G., & Morgenstern, R. (2020). The geomorphic impact of large landslides: A case-study of the actively moving alpine gardens landslide, fox glacier valley, west coast, new zealand. In *Egu general assembly conference abstracts* (p. 12411).

de Vilder, S., Massey, C., Lukovic, B., Taig, T., & Morgenstern, R. (2022). What drives landslide risk: Disaggregating risk analyses, an example from the franz josef and fox glacier valleys, new zealand. *Natural Hazards and Earth System Sciences Discussions*, 1–42. doi: https://doi.org/10.5194/nhess-2022-57

Drusch, M., Del Bello, U., Carlier, S., Colin, O., Fernandez, V., Gascon, F., ... others (2012). Sentinel-2: Esa's optical high-resolution mission for gmes operational services. *Remote sensing of Environment*, *120*, 25–36. doi: https://doi.org/10.1016/j.rse.2011.11.026

Farr, T. G., Rosen, P. A., Caro, E., Crippen, R., Duren, R., Hensley, S., ... others (2007). The shuttle radar topography mission. *Reviews of geophysics*, *45*(2). doi: https://doi.org/10.1029/2005RG000183

Fayne, J. V., Ahamed, A., Roberts-Pierel, J., Rumsey, A. C., & Kirschbaum, D. (2019). Automated satellite-based landslide identification product for nepal. *Earth Interactions*, *23*(3), 1–21. doi: https://doi.org/10.1175/EI-D-17-0022.1

Fortin, M.-J., James, P. M., MacKenzie, A., Melles, S. J., & Rayfield, B. (2012). Spatial statistics, spatial regression, and graph theory in ecology. *Spatial Statistics*, *1*, 100–109. doi: https://doi.org/10.1016/j.spasta.2012.02.004

Froude, M. J., & Petley, D. N. (2018). Global fatal landslide occurrence from 2004 to 2016. *Natural Hazards and Earth System Sciences*, *18*(8), 2161–2181. doi:

https://doi.org/10.5194/nhess-18-2161-2018

Gariano, S., Rianna, G., Petrucci, O., & Guzzetti, F. (2017). Assessing future changes in the occurrence of rainfall-induced landslides at a regional scale. *Science of the total environment*, *596*, 417–426. doi: https://doi.org/10.1016/j.scitotenv.2017.03.103

GDAL/OGR contributors. (2021). GDAL/OGR geospatial data abstraction software library [Computer software manual]. Retrieved from `https://gdal.org`

Geudtner, D., Torres, R., Snoeij, P., Davidson, M., & Rommen, B. (2014). Sentinel-1 system capabilities and applications. In *2014 ieee geoscience and remote sensing symposium* (p. 1457-1460). doi: 10.1109/IGARSS.2014.6946711

Glenn, N. F., Streutker, D. R., Chadwick, D. J., Thackray, G. D., & Dorsch, S. J. (2006). Analysis of lidar-derived topographic information for characterizing and differentiating landslide morphology and activity. *Geomorphology*, *73*(1-2), 131–148. doi: https://doi.org/10.1016/j.geomorph.2005.07.006

Gorelick, N., Hancher, M., Dixon, M., Ilyushchenko, S., Thau, D., & Moore, R. (2017). Google earth engine: Planetary-scale geospatial analysis for everyone. *Remote sensing of Environment*, *202*, 18–27. doi: https://doi.org/10.1016/j.rse.2017.06.031

Griffiths, J. S. (2018). Mass movement. In P. T. Bobrowsky & B. Marker (Eds.), *Encyclopedia of engineering geology* (pp. 597–604). Cham: Springer International Publishing. doi: https://doi.org/10.1007/978-3-319-73568-9_196

Guha-Sapir, D., Vos, F., Below, R., & Ponserre, S. (2012). Annual disaster statistical review 2011: the numbers and trends.

Harris, C. R., Millman, K. J., van der Walt, S. J., Gommers, R., Virtanen, P., Cournapeau, D., ... others (2020). Array programming with numpy. *Nature*, *585*(7825), 357–362. doi: https://doi.org/10.1038/s41586-020-2649-2

Heckmann, T., Schwanghart, W., & Phillips, J. D. (2015). Graph theory—recent developments of its application in geomorphology. *Geomorphology*, *243*, 130–146. doi: https://doi.org/10.1016/j.geomorph.2014.12.024

Hong, Y., Adler, R., & Huffman, G. (2007). Use of satellite remote sensing data in the mapping of global landslide susceptibility. *Natural hazards*, *43*(2), 245–256. doi: https://doi.org/10.1007/s11069-006-9104-z

Hungr, O., Leroueil, S., & Picarelli, L. (2014). The varnes classification of landslide types, an update. *Landslides*, *11*(2), 167–194. doi: https://doi.org/10.1007/s10346-013-0436-y

Jones, E., Mirus, B., Schmitt, R., Baum, R., Burns, W., Crawford, M., ... others (2019). Summary metadata—landslide inventories across the united states. *US Geological Survey data release*. doi: https://doi.org/10.5066/P9E2A37P

Lary, D. J., Alavi, A. H., Gandomi, A. H., & Walker, A. L. (2016). Machine learning in geosciences and remote sensing. *Geoscience Frontiers*, *7*(1), 3–10. doi: https://doi.org/10.1016/j.gsf.2015.07.003

Liu, J. G., & Mason, P. J. (2013). *Essential image processing and gis for remote sensing*. John Wiley & Sons.

Macara, G. (2016). The climate and weather of west coast. *NIWA Science and Technology Series 72*.

Manconi, A., Kourkouli, P., Caduff, R., Strozzi, T., & Loew, S. (2018). Monitoring surface deformation over a failing rock slope with the esa sentinels: Insights from moosfluh instability, swiss alps. *Remote Sensing*, *10*(5), 672. doi: https://doi.org/10.3390/rs10050672

Maxwell, A. E., Warner, T. A., & Fang, F. (2018). Implementation of machine-learning classification in remote sensing: An applied review. *International Journal of Remote Sensing*, *39*(9), 2784–2817. doi: https://doi.org/10.1080/01431161.2018.1433343

Mondini, A. C., Santangelo, M., Rocchetti, M., Rossetto, E., Manconi, A., & Monserrat, O. (2019). Sentinel-1 sar amplitude imagery for rapid landslide detec-

tion. *Remote sensing*, *11*(7), 760. doi: https://doi.org/10.3390/rs11070760

Pal, M. (2005). Random forest classifier for remote sensing classification. *International journal of remote sensing*, *26*(1), 217–222. doi: https://doi.org/10.1080/01431160412331269698

Paranjape, R. B., Rangayyan, R. M., & Morrow, W. M. (1994). Adaptive neighborhood mean and median image filtering. *Journal of Electronic Imaging*, *3*, 360-367. doi: https://doi.org/10.1117/12.180118

Pedregosa, F., Varoquaux, G., Gramfort, A., Michel, V., Thirion, B., Grisel, O., ... others (2011). Scikit-learn: Machine learning in python. *the Journal of machine Learning research*, *12*, 2825–2830.

Plank, S., Twele, A., & Martinis, S. (2016). Landslide mapping in vegetated areas using change detection based on optical and polarimetric sar data. *Remote Sensing*, *8*(4), 307. doi: https://doi.org/10.3390/rs8040307

Promper, C., Gassner, C., & Glade, T. (2015). Spatiotemporal patterns of landslide exposure–a step within future landslide risk analysis on a regional scale applied in waidhofen/ybbs austria. *International journal of disaster risk reduction*, *12*, 25–33. doi: https://doi.org/10.1016/j.ijdrr.2014.11.003

Rosser, B., Dellow, S., Haubrock, S., & Glassey, P. (2017). New zealand's national landslide database. *Landslides*, *14*(6), 1949-1959. doi: https://doi.org/10.1007/s10346-017-0843-6

Seneviratne, S., Nicholls, N., Easterling, D., Goodess, C., Kanae, S., Kossin, J., ... others (2012). Changes in climate extremes and their impacts on the natural physical environment.
doi: https://doi.org/10.7916/d8-6nbt-s431

Spoto, F., Sy, O., Laberinti, P., Martimort, P., Fernandez, V., Colin, O., ... Meygret, A. (2012). Overview of sentinel-2. In *2012 ieee international geoscience and remote sensing symposium* (p. 1707-1710). doi: 10.1109/IGARSS.2012.6351195

Stumpf, A., & Kerle, N. (2011). Object-oriented mapping of landslides using random forests. *Remote sensing of environment*, *115*(10), 2564–2577. doi: https://doi.org/10.1016/j.rse.2011.05.013

Tarboton, D. G. (1997). A new method for the determination of flow directions and upslope areas in grid digital elevation models. *Water resources research*, *33*(2), 309–319. doi: https://doi.org/10.1029/96WR03137

Tarrio, K., Tang, X., Masek, J. G., Claverie, M., Ju, J., Qiu, S., ... Woodcock, C. E. (2020). Comparison of cloud detection algorithms for sentinel-2 imagery. *Science of Remote Sensing*, *2*, 100010. doi: https://doi.org/10.1016/j.srs.2020.100010

Torres, R., Snoeij, P., Geudtner, D., Bibby, D., Davidson, M., Attema, E., ... others (2012). Gmes sentinel-1 mission. *Remote Sensing of Environment*, *120*, 9–24. doi: https://doi.org/10.1016/j.rse.2011.05.028

Turkar, V., Deo, R., Rao, Y. S., Mohan, S., & Das, A. (2012). Classification accuracy of multi-frequency and multi-polarization sar images for various land covers. *IEEE Journal of Selected Topics in Applied Earth Observations and Remote Sensing*, *5*(3), 936-941. doi: https://doi.org/10.1109/JSTARS.2012.2192915

Tzouvaras, M., Danezis, C., & Hadjimitsis, D. G. (2020). Small scale landslide detection using sentinel-1 interferometric sar coherence. *Remote Sensing*, *12*(10), 1560. doi: https://doi.org/10.3390/rs12101560

Van Den Eeckhaut, M., Kerle, N., Poesen, J., & Hervás, J. (2012). Object-oriented identification of forested landslides with derivatives of single pulse lidar data. *Geomorphology*, *173*, 30–42. doi: https://doi.org/10.1016/j.geomorph.2012.05.024

Zekoll, V., Main-Knorn, M., Louis, J., Frantz, D., Richter, R., & Pflug, B. (2021). Comparison of masking algorithms for sentinel-2 imagery. *Remote Sensing*,

13(1), 137. doi: https://doi.org/10.3390/rs13010137

Zhao, C., & Lu, Z. (2018). Remote sensing of landslides—a review. *Remote Sensing*, *10*(2), 279. doi: https://doi.org/10.3390/rs10020279

Zhong, C., Liu, Y., Gao, P., Chen, W., Li, H., Hou, Y., ... Ma, H. (2020). Landslide mapping with remote sensing: challenges and opportunities. *International Journal of Remote Sensing*, *41*(4), 1555–1581. doi: https://doi.org/10.1080/01431161.2019.1672904

Zink, M., Bachmann, M., Brautigam, B., Fritz, T., Hajnsek, I., Moreira, A., ... Krieger, G. (2014). Tandem-x: The new global dem takes shape. *IEEE Geoscience and Remote Sensing Magazine*, *2*(2), 8–23. doi: https://doi.org/10.1109/MGRS.2014.2318895